OPTIMAL PLACEMENT OF HIGH-CHANNEL VISUAL PROSTHESES IN HUMAN RETINOTOPIC VISUAL CORTEX

Rick van Hoof[1]*, Antonio Lozano[2]*, Feng Wang[2]*, P. Christiaan Klink[2,3], Pieter R. Roelfsema[2, 4, 5, 6], Rainer Goebel[1,7]

[1] *Department of Cognitive Neuroscience, Maastricht University, Maastricht, the Netherlands*
[2] *Department of Vision and Cognition, Netherlands Institute for Neuroscience, Amsterdam, the Netherlands.*
[3] *Experimental Psychology, Helmholtz Institute, Utrecht University, Utrecht, the Netherlands*
[4] *Department of Integrative Neurophysiology, VU University, Amsterdam, the Netherlands*
[5] *Department of Psychiatry, Academic Medical Centre, Amsterdam, the Netherlands*
[6] *Laboratory of Visual Brain Therapy, Sorbonne Université, INSERM, CNRS, Paris, France*
[7] *Maastricht Brain Imaging Centre, Maastricht University, Maastricht, the Netherlands*

* contributed equally

ABSTRACT

Recent strides in neurotechnology offer hope for restoring vision in individuals afflicted with blindness due to early visual pathway damage. We present a comprehensive method to optimize electrode placement for visual prostheses, with the objective of aligning with predetermined phosphene distributions. Our approach relies on individual anatomy data to minimize discrepancies between simulated and target phosphene patterns. While tailored for a 1000-channel 3D electrode array in V1, our algorithm is versatile, potentially accommodating any electrode design. Notably, our results show individually optimized placements outperform average brain solutions, underscoring the significance of anatomical specificity. Nevertheless, challenges persist in achieving comprehensive visual field coverage owing to current electrode constraints. We propose potential solutions involving multiple arrays to address this limitation. Additionally, considering intracranial vasculature constraints in future iterations could refine the optimization process. Our openly accessible software streamlines the refinement of surgical procedures and facilitates simulation studies, offering a realistic exploration of electrode design possibilities.

Keywords neurotechnology · visual prosthetics · electrode placement · retinotopy · phosphene mapping · population receptive field maps · magnetic resonance imaging · primary visual cortex · Bayesian optimization · simulation software · intracortical electrodes

1 INTRODUCTION

Advances in neurotechnology are making it increasingly feasible to directly stimulate the brain and restore lost functions. One challenge is the restoration of a rudimentary form of vision in patients that have become completely blind due to damage in their early visual pathways (Brindley & Lewin, 1968; Dobelle et al., 1974; Farnum & Pelled, 2020; Nowik et al., 2020; Roelfsema, 2020; Schmidt et al., 1996). The typical approach is to replace a part of the visual pathway with a brain-computer-interface (or visual prosthetic implant) that translates a camera feed into patterned electrical signals that are used to directly stimulate the brain. Such stimulation of the early visual pathways (retina, optic nerve, thalamus, or visual cortex) elicits dot-like visual sensations with fixed spatial locations known as phosphenes (Brindley & Lewin, 1968; Dobelle et al., 1976; Lee et al. 2000; Maynard 2001; Schmidt et al., 1996). In intact visual systems, the spatial location of a phosphene corresponds to the stimulated neuron's receptive field, the location of the visual field where visual stimuli evoke a response. Receptive fields are predictably organized to represent the visual world in a way that replicates the topography of the retina across several brain areas (i.e., they have a retinotopic organization). This organization is comparable across individuals, but some variability does exist (Benson et al., 2018a, 2022). Patterns of phosphenes that together form shapes can be evoked by stimulating several electrodes simultaneously (X. Chen et al., 2020; Dobelle et al., 1976) or in close temporal proximity (Beauchamp et al., 2020; Bosking et al., 2022; Oswalt

et al., 2021). This way, phosphene patterns that are created in real-time, based on a (preprocessed) camera feed, will be able to help blind individuals recover some visual functions that were lost or severely impaired after becoming blind (Fernández et al., 2021). At this moment, visual prosthetics developments are typically focused on patients with late-onset blindness because since they have experienced vision at one point in their life, 1) they are most aware of what they are missing and often eager to regain even a rudimentary form of vision; 2) their visual brain is thought to have developed relatively normally and contain the required connectivity for this approach to work (Heitmann et al., 2023). One major question for all visual neuroprosthetic approaches is where to interface with the brain. The broad retinotopic organization of the visual brain puts forward many potential targets for implantation, each with their own challenges and phosphene location predictability. Here, we present a comprehensive method to optimize the selection of electrode placement location so that the locations where the implant can evoke phosphenes (i.e., its "phosphene map"; PM in figure 1D) matches a preset desired distribution as closely as possible.

In the 1970s, Dobelle et al. (1974) were the first to connect a camera system to a set of surface electrodes on the medial side of the occipital lobe. However, modern intracortical electrodes offer several advantages over surface electrodes. Phosphenes can be evoked with currents that are two orders of magnitude lower because intracortical stimulation electrodes are much closer to their target neurons (Schmidt et al., 1996). Intracortical electrodes can also reach neurons in areas that are contained within folded sulci. The calcarine sulcus of the human brain, for instance, contains a sizable fraction of primary visual cortex (V1) and would be practically unreachable for stimulation by large surface electrodes. Notably, neurons with RFs representing the periphery of visual space (i.e., those with larger eccentricities) are located deep inside the calcarine fissure/V1 (Wandell et al., 2007) and the amount of tissue disturbed by attempts to stimulate them with surface electrodes would likely be an issue.

Additionally, the number and distribution of stimulation electrodes covering visual space are important determinants. More complex phosphene patterns will require a larger number of electrodes and larger patterns require a broader coverage of visual space. Recent developments in image processing have produced information reduction algorithms that allow the most relevant features of a scene to be selectively converted into efficient phosphene patterns. In theory, prostheses should allow crucial every-day life activities such as accurate emotion expression recognition (Bollen et al., 2019), navigation (de Ruyter van Steveninck et al., 2022; Lu et al., 2014; Perez-Yus et al., 2017; Vergnieux et al., 2017; L. Wang et al., 2008), object recognition (Li et al., 2018; Lu et al., 2014; Macé et al., 2015; Sanchez-Garcia et al., 2018; Xia et al., 2015) and even motion detection (X. Chen et al., 2020; Perez-Yus et al., 2017) to be reestablished after vision loss.

The functional properties of artificial vision with different sets of phosphenes, corresponding to different prosthetic devices, can be studied in seeing volunteers using phosphene simulations. To date, such studies have often assumed high density, uniformly spaced, full field covering phosphene configurations (Avraham et al., 2021; Bollen et al., 2019; S. Chen et al., 2009; Sanchez-Garcia et al., 2020; Steveninck et al., 2020; J. Wang et al., 2021), which is a highly unlikely assumption given the anatomy and functional organization of the human brain. Current state-of-the-art prostheses only cover a small portion of the visual field (Fernández et al., 2021; Niketeghad & Pouratian, 2019), which is often a hardware limitation. With these limitations in mind, it is conceivable that different types of daily activities might require different phosphene configurations. A multi-functional visual prosthesis thus requires a careful selection of electrode configurations. For example, a dense foveal coverage would be useful for reading, or recognizing an object in front of you, while peripheral vision may be important for context awareness during navigation. In order to realistically study the functional properties of phosphene vision, a biologically and technologically plausible simulation of stimulation-evoked phosphenes is crucial (Van Der Grinten, de Ruyter van Steveninck, Lozano et al., 2024).

An ideal phosphene coverage throughout the visual field would likely require many stimulation sites in a brain structure that encodes the entire visual field. Candidate structures are the retina, lateral geniculate nucleus (LGN) and cortical areas V1 to higher order regions like V2, V3, V4 and hMT. It remains unclear how phosphenes evoked by stimulation of different hierarchical areas of the visual cortex perceptually combine (Schiller et al., 2011; Schmidt et al., 1996). Contemporary approaches therefore typically target a single functional area. The LGN represents the entire visual space in a relatively small volume of brain tissue, but because of its location deep in the brain, stimulating LGN would require long electrode shanks with a high number of densely placed electrodes at the tip.

The primary visual cortex (V1) lies more superficial, making it an interesting candidate for a visual prosthesis. The functional organization of basic visual features such as columnar orientation selectivity and color selectivity is well established in V1 and its position early in the visual processing hierarchy might allow higher level areas in to process more complex visual features, such as motion (Salzman et al., 1990) or faces (Mundel et al., 2003) in a relatively natural way.

The feasibility of using large-scale V1 stimulation to generate phosphene-based pattern vision was recently investigated in rhesus monkeys (Chen et al., 2020, 2023) with a 1,024-channel count cortical prosthesis. Human cortex, however, has a lot more gyrification and substantial individual differences in the surface area of visual cortices (Benson et al., 2021). The functional organization of early visual cortex is, however, relatively predictable across individuals as long as the individual anatomy is known (Benson & Winawer, 2018; Rosenke et al., 2021; L. Wang et al., 2015). The ability to derive function from anatomy is especially important in blind patients, as conventional fMRI localizers based on visual input cannot be used. The functional organization of an individual's brain, together with the electrode design and placement, will ultimately determine what kind of phosphene maps a visual prosthesis can generate.

Our method to optimize the placement of electrodes for a visual prosthesis incorporates 1) the individual anatomy that predicts functional maps, 2) flexibility in electrode design, and 3) a preset phosphene map one aims to obtain with the prosthesis. The ideal visual prosthesis would cover the entire visual field with appropriate spatial resolution. Here, we explore the feasibility of this ideal within a set of practical constraints. Our pipeline is open-source and automatically finds the electrode configuration that optimally matches a preset 'ideal' phosphene map within these constraints. Because the pipeline uses the individual brain anatomy as a starting point, it can also be used in blind subjects after obtaining a simple anatomical MRI scan. The optimal location and insertion angles of configurable electrode array models are determined with a Bayesian optimization procedure. This algorithm efficiently minimizes a cost function that considers the electrode yield in grey matter, the visual field coverage of the phosphene distribution, and the relative entropy between the preset target phosphene map and the predicted phosphene map based on the current implantation parameters. In the example implementation we present here, model parameters were optimized for a 3D electrode array containing a thousand contact points equally distributed over a 10x10 grid of contact points aimed to be implanted in V1. The general procedure, however, allows for any electrode design and can easily be applied to other or multiple brain areas. We validated our method on 362 human hemispheres using anatomical and retinotopy data from the Human Connectome Project 7T retinotopy dataset (Benson et al., 2018b).

2 METHODS

2.1 Preprocessing of the Human Connectome Project 7T retinotopy dataset

Data was obtained from the Human Connectome Project 7T retinotopy dataset (Benson et al., 2018). T1-weighted (T1w) and T2-weighted (T2w) structural scans at 0.7-mm isotropic resolution were processed using the FreeSurfer image analysis suite (version 7.2; http://surfer.nmr.harvard.edu). Subject brains were inflated and aligned to FreeSurfer's anatomical *fsaverage* atlas.

The inferences made in this work are based on the retinotopic data described by Benson et al., (2018). In brief, MRI data was acquired using a Siemens 7T Magnetom actively shielded scanner and a 32-channel receiver coil array with a single channel transmit coil (Nova Medical, Wilmington, MA) at a 1.6mm isotropic resolution and 1s TR (multiband acceleration 5, in-plane acceleration 2, 85 slices). The population receptive field (pRF) maps describe the location and the size of the receptive field for each 1mm isotropic voxel (see Benson et al. (2018) for descriptions of pRF models used). pRF surface maps based on empirical data in Freesurfer fsaverage space were warped to individual space using Freesurfer's *mri_surf2surf* function. Bayesian inference of the retinotopic maps was performed using Neuropythy's *register_retinotopy* command (https://github.com/noahbenson/neuropythy). This procedure harmonizes the anatomical inference of the pRFs, the Benson 2014 atlas (Benson et al., 2014) and experimental data (Benson et al., 2018) comprised of retinotopic responses to visual stimuli up to 8 degrees eccentricity. Note that the Benson 2014 atlas predicts maps up to 90 degrees eccentricity, however only the inner 20 degrees of eccentricity in V1, V2, and V3 have been empirically validated.

2.2 Pipeline for optimization of electrode placement

Our strategy to optimize electrode placement is to minimize the difference between a 'target' phosphene distribution (TP) and a 'predicted' phosphene map (PP) that we infer from virtual placement of electrodes into a brain model with probabilistic or measured retinotopic maps. This difference was quantified and minimized by calculating the loss with a Bayesian search algorithm (scikit; Pedregosa et al., 2011). An example of the electrode design (and its simplification) used for the simulations is displayed in figure 1A. The main input variables of the optimization function were the angles *alpha* (pitch) and *beta* (yaw), which define the insertion trajectory of the virtually placed implant. This insertion trajectory was determined by finding the intersection between the insertion point on the cortical sheet and the

centroid of the calcarine sulcus (CS) at the angles *alpha* and *beta* (Figure 1A-B). The centroid, or geometric center, was calculated using the medians along the three dimensions of the CS volume. Importantly, the CS has been reported to be a reliable estimate of the location and total volume of the human primary visual (Gilissen & Zilles, 1996). To test whether this is also the case in the HCP dataset, the CS volume was determined by Freesurfer's cortical parcellation algorithm (Desikan-Killiany Atlas) and compared to the volume of V1 (all voxels in the cortical ribbon of the V1-parcel determined by the pRF model), see supplementary figure S1. The range of insertion angles were restricted so that the insertion trajectory cannot intersect with the other hemisphere, and it excludes unrealistic surgical approaches (e.g. insertion in an anterior - posterior direction).

For many combinations of angles, a portion of the electrode grid would end up outside of the cortex. In case any electrode was out of bounds, the configuration was flagged as invalid, and a penalty was assigned in the optimization procedure. To circumvent this, an extra parameter (*shank offset)* was added to the optimization function to enable the distance between the insertion point on the cortical surface and the first contact point on the electrode shank to vary (Figure 1A). To vary cortical depth, the final parameter *shank length* was included in the search for optimal electrode coverage, density and yield (Figure 1A). We constrained electrodes to not exceed a cortical depth of 8cm, as the average width and length of HCP brains are about 17cm and 13cm (Yang et al., 2020). Furthermore, the search can be used to optimally place electrodes in a specific region of interest. Here, we targeted V1 and added a penalty when contact points were located outside V1. Neurons in V1 have a smaller receptive field size compared to higher visual areas (Benson et al., 2021), potentially allowing denser phosphene maps.

For each set of parameters, or cycle of the optimization pipeline (Figure 2), the electrode-grid is virtually positioned to match the trajectory set by the insertion angles. The predicted phosphene map is then extracted from the intersection of the electrode coordinates and the voxels of the retinotopic map. Each individual electrode that is located in a retinotopically defined map yields a phosphene on a 500-by-1000-pixel image-grid, ranging up to 90 degrees visual angle. To simplify the simulation, we fix the spread of stimulation current to the voxel size of the retinotopic map ($1mm^3$). Phosphenes are modeled as 2-D Gaussian spots of light with standard deviation ranging from 0.2 up to 3 visual degrees, depending on the cortical magnification factor and a simulated stimulation amplitude of 100 micro-amps (Tehovnik et al., 2005; Wang et al., 2008). Finally, the process is repeated for a new set of parameters up to 100 times (separately for each hemisphere). The entire procedure is illustrated by the images in figure 1 and the flowchart diagram in figure 2.

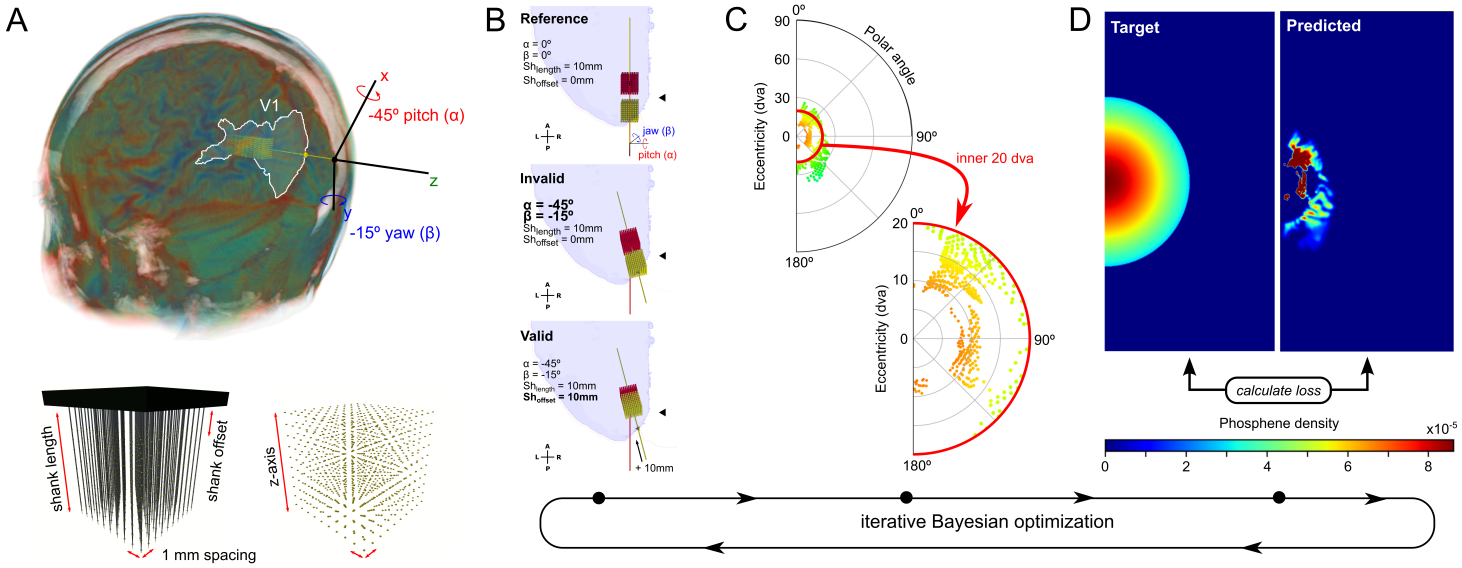

Figure 1. Overview of electrode optimization pipeline. The Bayesian search algorithm determines the next set of parameters based on a loss function with several components (see Methods), and the process is repeated until the optimal set of parameters is found for a specific target phosphene configuration. A) illustration of electrode placement (top) and electrode-grid configuration parameters (bottom). B) The red grid only serves as a reference and is centered on the center of the left calcarine sulcus (black triangles). The implant position (yellow grid) is calculated based on alpha (pitch) and beta (yaw) relative to the reference grid. For a new set of parameters, the resulting configuration can be either valid (left) or invalid (center) when contact points are located outside of the brain. In the 'valid' example, the contact point closest to the base is located 10mm from the point where the shank penetrates the cortex. C) Each contact point potentially evokes a phosphene in the polar angle plot. The individual phosphenes are modeled as 2-D Gaussians on a 500-by-1000-pixel phosphene map**.** Color codes for eccentricity. D) One of the loss terms is the Hellinger distance between the probability distributions of the simulated phosphene map (left) and the target phosphene map (right).

2.3 Bayesian optimization

Bayesian optimization has become an attractive method to optimize expensive to evaluate black box functions which are derivative-free and possibly noisy (Shahriari et al., 2016). The algorithm iteratively evaluates a probabilistic model for which a cheap probability function f based on the posterior distribution is optimized before sampling the next point. The function objective is considered as a random function (a stochastic process) on which a prior is placed. Here, the prior is defined by a Gaussian process capturing our beliefs about the function behavior. Function evaluations are treated as data and used to update the prior to form the posterior distribution over the objective function. The convergence of the optimization algorithm was accelerated by setting an initial sampling point for which it was known that the resulting grid would hit some portion of V1. We chose to position the center of the electrode grid at the centroid of the calcarine sulcus with initial parameters 0° *alpha*, 0° *beta,* 20mm *shank length* and 25mm *shank offset*. The model can also be run without such prior knowledge of the objective function, but it will likely take more iterations to converge.

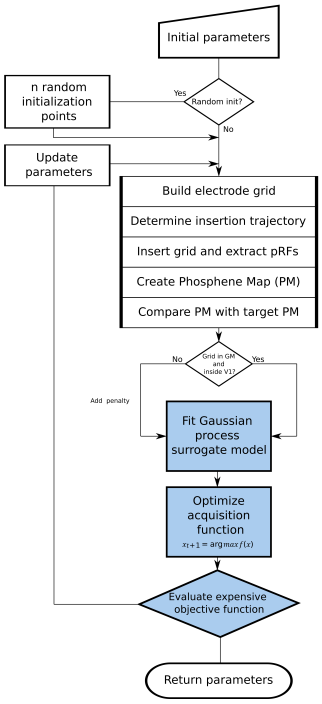

Figure 2. Flowchart diagram Bayesian optimization pipeline. This diagram provides an overview of the virtual electrode placement pipeline. Rectangular boxes indicate processing steps diamond shapes indicate model decisions.

2.4 Loss function

The loss function comprised three linearly weighted terms that together indicate the difference between a desired phosphene map and the phosphene map predicted from sampling the pRF parameters at the location of the 1000 simulated electrodes in the brain. Below, we explain each loss term and its meaning in the context of the optimization goals. We chose to emphasize the contribution of visual field coverage and phosphene distribution (by a factor of 10) relative to the absolute number of electrodes in V1. However, depending on the desired outcome, the weights (a, b and c) of the loss terms can be preset.

$$Loss = aDC + bY + cKL \tag{1}$$

2.4.1 Sørensen–Dice coefficient

The dice coefficient (*DC*) is a measure of overlap between two datasets. DC was computed on the binarized target phosphene map (TP) and a binarized version of the predicted phosphene map (PP). Each map's pixels are set to 1 if they contain phosphene activation and 0 if they do not. |TP| and |PP| represent the number of elements in each set. The Sørensen index equals twice the number of elements common to both sets divided by the sum of the number of elements in each set. Dice is included to obtain phosphene maps that are localized in the desired visual region.

$$DC = \frac{2|TP \cap PP|}{|TP| + |PP|} \tag{2}$$

2.4.2 Yield

Yield indicates the proportion of electrodes that can evoke a phosphene. We aim this to be as high as possible, thus allowing the implant to achieve high spatial resolution. Contact points outside of the targeted region are penalized by adding a constant to this loss term.

$$Y = \frac{n_{hits}}{n_{contactpoints}} \tag{3}$$

2.4.3 Hellinger distance

The Hellinger distance (*H*) quantifies the similarity between two probability distributions and is defined as the square root of the expected squared difference between the square roots of the probability distributions.

$$H(P, Q) = \sqrt{\sum \left(\sqrt{P} - \sqrt{Q}\right)^2} \tag{4}$$

Hellinger distance is especially suitable for comparing normalized discrete probability distributions in machine learning as it is restricted to the range between 0 and 1. *P* refers to the probability distribution of the target phosphenes, and Q to the distribution of predicted phosphenes. The maximum distance 1 is achieved when *P* assigns probability 0 to every set to which *Q* assigns a positive probability, and vice versa. *H* will reward parameter sets for which the virtually implanted electrodes yield a phosphene map with the desired density distributions and penalize density distributions that diverge from the target map.

2.5 Phosphene maps

There is a clear (hardware-based) limit to the extent of visual field coverage within the parameters of the single electrode array we use here (see Figure 3 and 4). It is simply not realistic to expect full visual field coverage with limited spatial electrode coverage. In addition, different cognitive functions may differentially rely on different subregions of the visual field and individual patients may choose a visual field coverage that matches their preferences. Since the exclusive consideration of 'full coverage' does not provide sufficient insight into the procedure's accuracy in targeting specific subregions of the visual field, we tested the spatial specificity of our pipeline by targeting four distinct target coverages:

1. *full target*: dense representation starting from the fovea, covering 0-90° eccentricity.
2. *inner target*: dense representation starting from the fovea, covering 0-45° eccentricity.
3. *upper target*: dense representation around the fovea, covering 0-90° eccentricity and 0-45° polar angle of the upper visual field.
4. *lower target*: dense representation around the fovea, covering 0-90° eccentricity and 135-180 ° polar angle of the lower visual field (see figure 1D and figure 9 for reference).

Simulated phosphenes were scaled based on eccentricity and inspired by recently published phosphene simulation work (Van Der Grinten, de Ruyter van Steveninck, Lozano et al.,2024). Our simulations employed flattened cortical maps as described by Schwartz (1983) and the multi-area visuotopic map complexes in macaque striate and extra-striate cortex identified by Polimeni et al. (2006). Default parameters were taken from Horton and Hoyt's revision of the classic Holmes map (1991), but patient-specific maps or approximations of Benson et al.'s findings (Benson et al., 2018a) could be considered in future work. The cortical magnification factor (CMF) for each electrode location was computed to determine the degrees of visual angle covered per mm of tissue surrounding each electrode. Using a simulated stimulation amplitude of 100 micro-amps, the amount of tissue activated was estimated based on the function and parameters established by Tehovnik and Slocum (2007). CMF was then multiplied by the activated area to obtain the phosphene size in degrees of visual angle. To define the Gaussian's activation area, the phosphene size was divided by two, ensuring that 95% of the Gaussian's activation fell within the phosphene's radius. Finally, a Gaussian distribution was drawn for each phosphene using the calculated size.

2.6 pRF polar density estimation

Probability density functions (PDFs) of group average PMs were defined by computing a non-parametric kernel-density estimation (KDE) using SciPy 1.0 (Virtanen et al., 2020). The group average PMs were created by summing simulated phosphenes of the optimized electrode locations in all subjects. PMs were created separately for each region of interest (grey matter, V1, V2, V3). The polar plots in figure 5 and 6 allow a qualitative analysis of phosphene locations across subjects. Density was scaled by the maximum to allow for a fair comparison between regions of interest.

2.7 Group average electrode configuration

In addition to the individual approach, i.e. determine the best electrode configuration for each person individually, we also optimized electrode placement based on the average brain. Here, we applied the electrode optimization pipeline to the *fsaverage* brain and the group average retinotopy (averaged timecourse). Phosphene maps were then predicted for individuals either based on the ‘average’ or ‘individual’ parameter estimates. Results were compared to establish the potential benefits of an individual optimization approach (see figure 7).

2.8 Statistical analysis

Repeated Measures Individual Analysis of Variance (RMANOVA) and pairwise post-hoc Tukey’s multiple comparison tests were performed using Python library statsmodels v0.14.0 (Seabold & Perktold, 2010). The reported statistical results were Bonferroni corrected by dividing the significance levels by two (the number of individual ANOVA analyses) to correct for multiple comparisons.

3 RESULTS

Optimal electrode placement in primary visual cortex was determined for both hemispheres of 181 subjects from the HCP 7T dataset by minimizing the difference between a desired phosphene map (DPM) and predicted phosphenes from virtual electrode placements. The feasibility of obtaining maximal visual field coverage is illustrated using data from example subjects (figure 3 and 4). The average results over all individuals are then described using pRF/phosphene density distributions (figure 5 and 6) indicating the probability that a phosphene was evoked in a specific spatial location with the optimized placements parameters. Finally, we compared individualized optimization based on an individual’s own brain scan with the general optimization solution based on the group (fs)average brain (figure 7).

3.1 Standardized starting point for the Bayesian search space

In our sample of 181 individuals, we found that the volume of the calcarine sulcus (CS) correlated well with the volume of V1 in both hemispheres (Pearson correlation left hemisphere: $r = 0.95$, $p < 0.001$; right hemisphere $r = 0.87$, $p < 0.001$; figure S1). We used the centroid of the CS as a standardized anatomy based starting point for optimization (with alpha and beta insertion angles set to zero).

3.2 Phosphene maps from optimized electrode placements

We optimized electrode placements for a target phosphene density map with a coverage of 90 degrees and with a density that follows a Gaussian function, corresponding to the entire visual field. Figure 3 provides an example of the best possible placement for our electrode array design, using the trajectory constraints defined in 'Pipeline for optimization of electrode placement', the brain's anatomical dimensions, as well as the predicted phosphene density map. The optimal phosphene map reveals a densely populated area between the first 5 to 20 visual degrees, followed by a coherent spaced-out distribution at higher eccentricities. High eccentricities are notably absent, due to constraints of the electrode array and cortical layout.

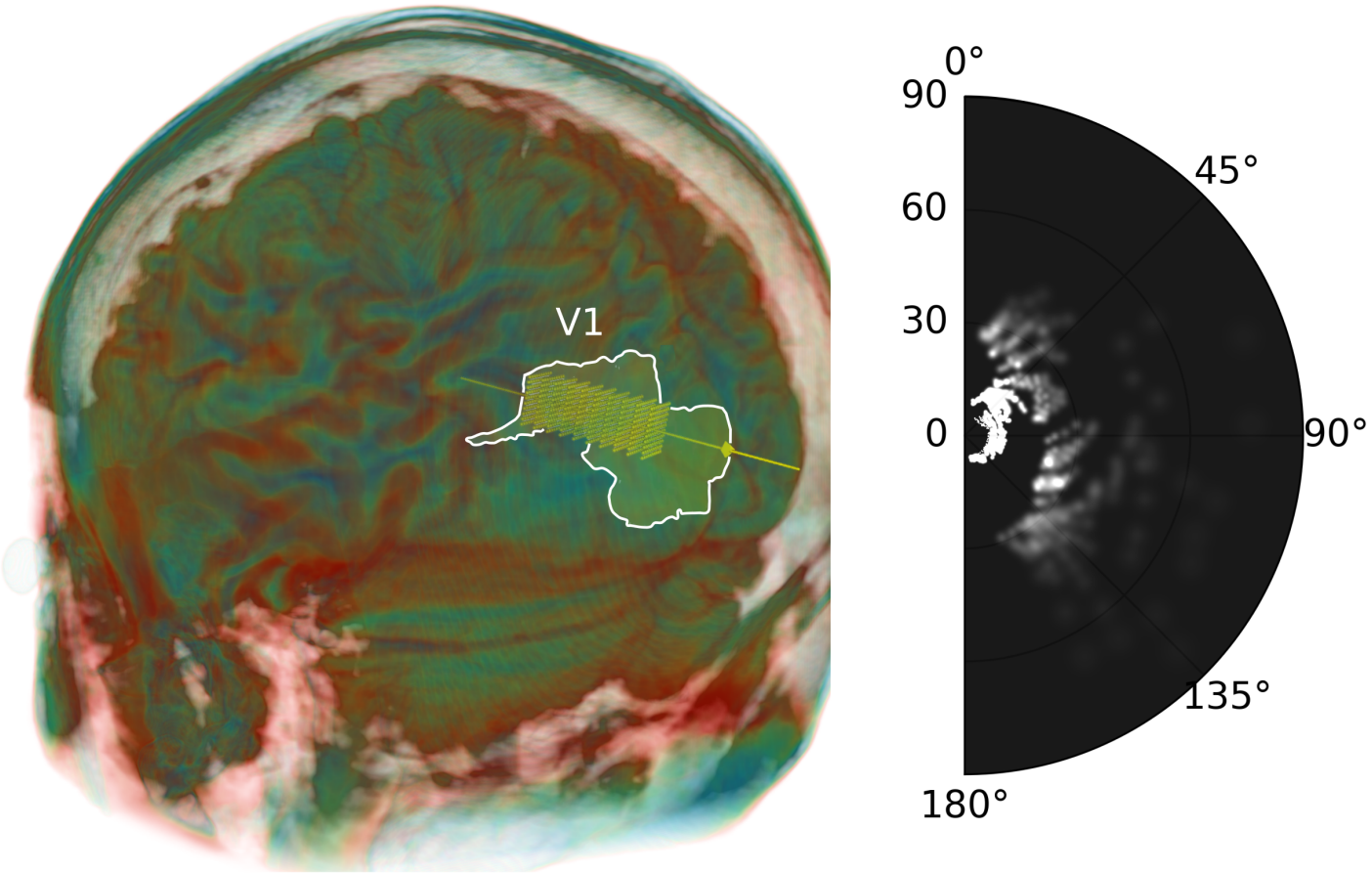

Figure 3. Phosphene configuration in an example subject. On the left the location of the electrodes after implantation are shown for parameters alpha=13, beta=-15, shank offset=13mm, shank length=24mm. V1 is indicated as the white ROI. The simulated phosphene map corresponding to the electrode locations is displayed on the right, where intensity depends on the number of overlapping phosphenes.

Figure 4 shows optimized phosphene locations in two subjects for the full visual field and the inner half of the visual field, along with the best configuration for the *fsaverage* brain. Repeated measures ANOVA revealed a significant interaction on *loss* between *target* and *hemisphere* ($F(3, 540) = 7.1$, $p < 0.001$). We also found a pronounced difference between *left* and *right* hemispheres for *full* target ($M = -0.05$, $p < 0.001$), *lower* target ($M = -0.10$, $p < 0.001$) and *upper* target ($M = -0.07$, $p < 0.001$). Loss was lower for the right hemisphere for all targets, except the inner target (see Figure 4C).

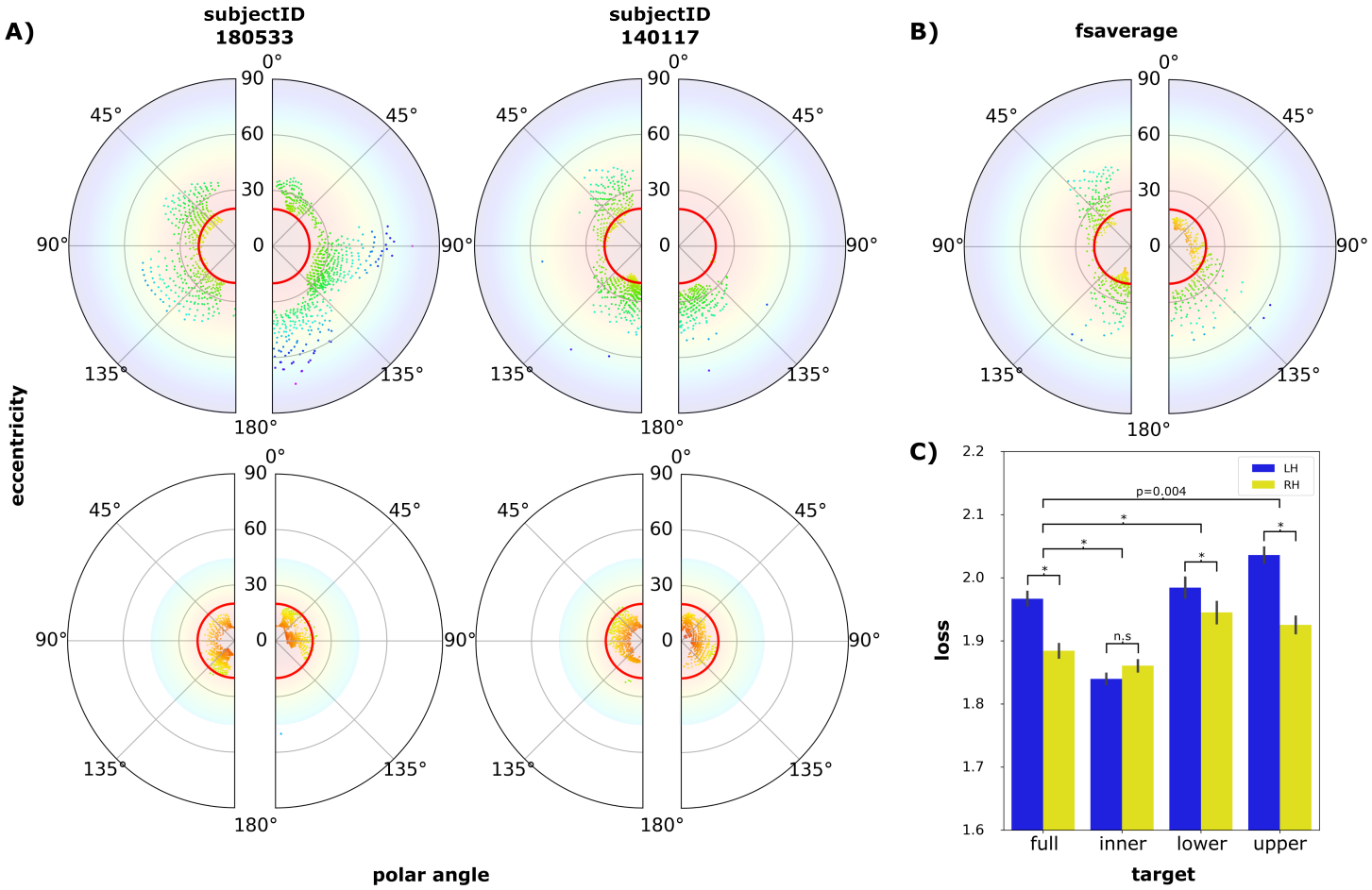

Figure 4. Comparison of individually optimized electrode configurations for the full visual field and foveal target. A) The top row shows phosphene locations in two randomly selected subjects for eccentricities up to 90 degrees (top row) and 45 degrees (bottom row). B) The polar plots show optimization results for the averaged pRF from all subjects in the fsaverage brain (top). C) The barchart (bottom right) depicts loss in all subjects in both hemispheres per target. Error bars indicate standard error. [* = p<0.001].

Optimization variability across the population was further evaluated with group-average probability density functions (PDFs) of predicted phosphenes across the visual field. In figure 5 and 6, PDFs are shown per target phosphene map across the regions of interest. We observed a fairly symmetrical phosphene peak distribution across hemispheres, with most phosphenes located quite central in the visual field. Phosphenes obtained for the upper and lower target maps were mostly located in the expected visual quadrants, however a relatively large proportion of these phosphenes came from electrode contacts in V2 and V3. This indicates that even when the algorithm prefers to place the grid in V1 for these target regions, frequently no solution could be found where all 1000 electrodes are placed in V1.

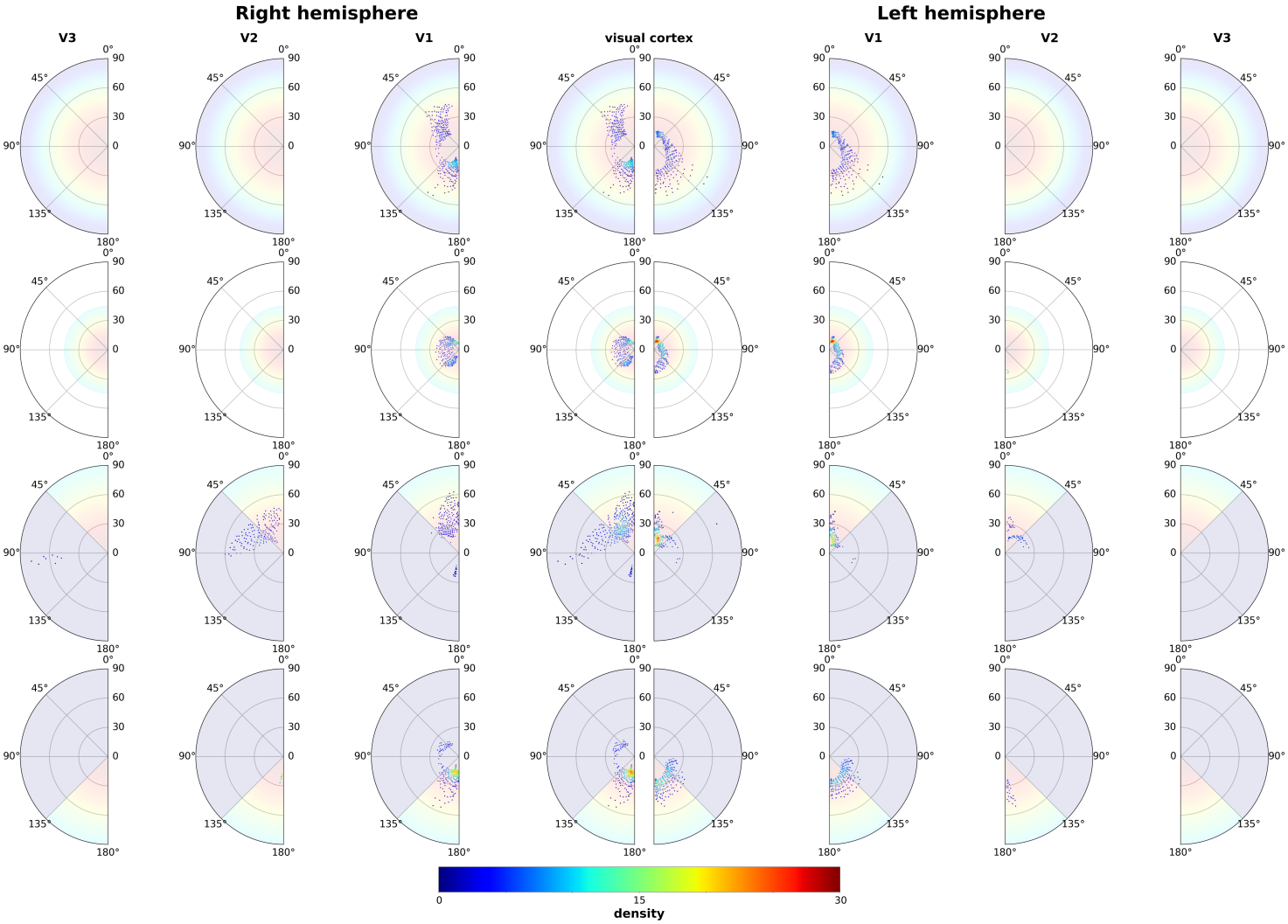

Figure 5. pRF density polar plots in the fsaverage brain. Results after running the pipeline on subject average pRF maps projected on the fsaverage brain. The color indicates the density (as determined by Gaussian KDE) of simulated phosphenes in visual space. For reference, the target PM is shown on the background of each plot.

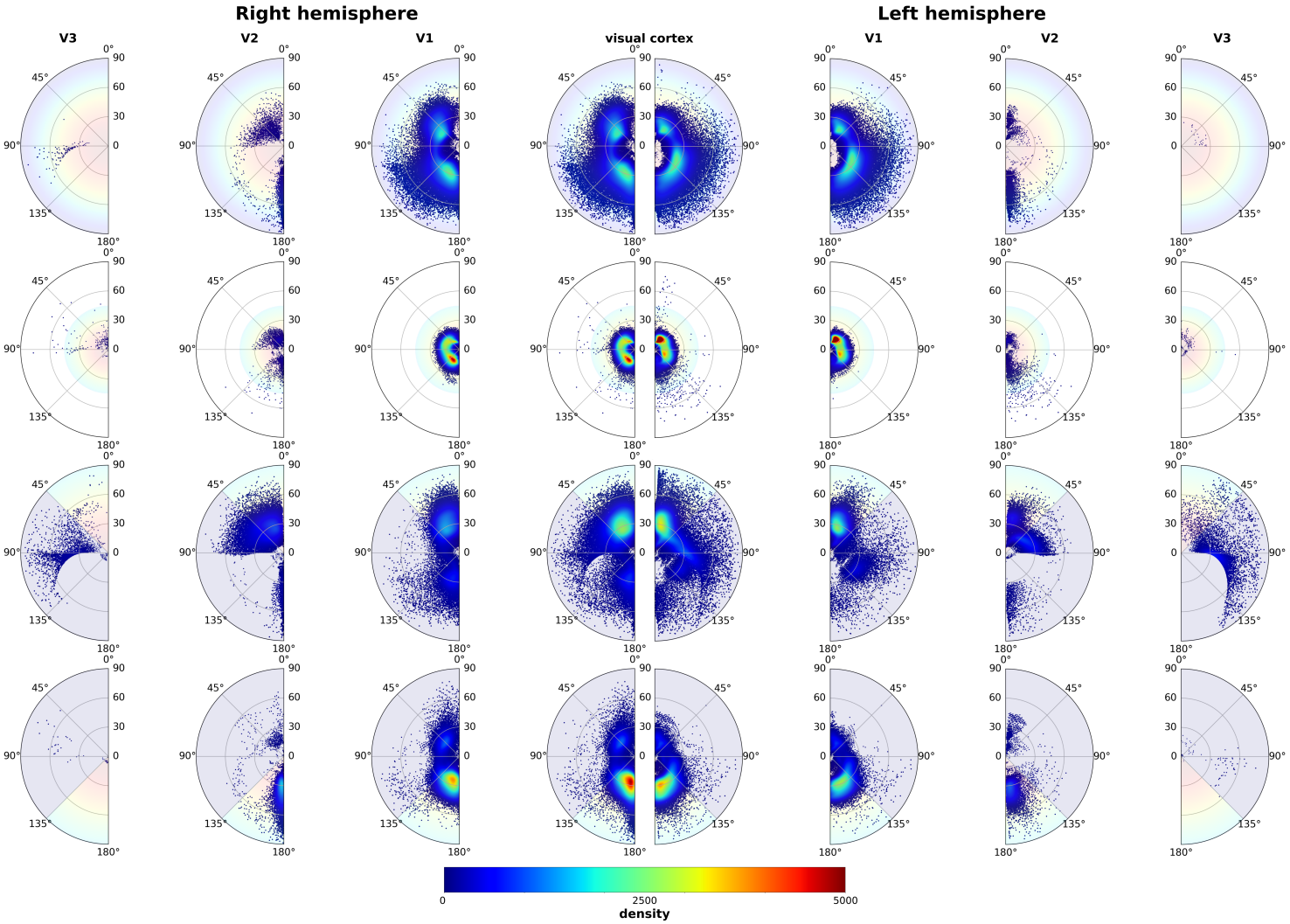

Figure 6. Group average pRF density polar plots. The center plots show a summary of all pRF locations in either left or right hemisphere after optimizing electrode configurations in all subjects. The color indicates the density (as determined by Gaussian KDE) of simulated phosphenes in visual space. As a reference, the target PM is shown on the background of each plot.

3.3 Group average optimization versus individual optimization

For a less computationally expensive, and thus faster way to design an electrode grid, we can optimize the placement of electrodes on the average brain and then virtually implant this configuration in all individuals. In figure 7 this group average approach is compared with the results from the individualized optimization approach. Each element of the loss function is shown separately for a more detailed description of differences in visual coverage. Post hoc comparisons using the Tukey HSD test indicated that the individually optimized approach significantly outperformed the average approach for phosphene yield ($M = 0.03$, $p < 0.001$), phosphene map coverage ($M = 0.18$, $p < 0.001$), as well as Hellinger distance ($M = 0.08$, $p < 0.001$). See supplementary materials (figure S4) for single-subject examples.

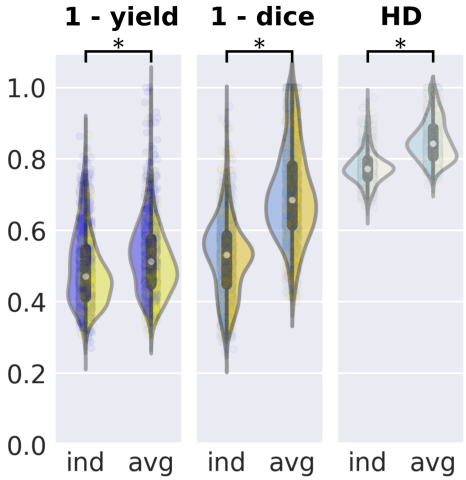

Figure 7. Superior visual coverage for individually fine-tuned electrode placement. The violin plots describe the three loss terms with each half representing results for the left or right hemisphere. Configurations based on individually optimized parameters (ind) result in significantly more electrodes successfully placed in V1, higher phosphene coverage and a more accurate density distribution compared to an average electrode configuration (avg)
[* = p<0.001].

4 DISCUSSION

Restoring even a rudimentary form of vision in blind patients is an ambitious aim for neuroscience and neural engineering that has recently gained a lot of attention. Visual prostheses that interface directly with the brain may one day be a realistic treatment option for blindness that results from damage to the early visual pathways (Fernández et al., 2021; Roelfsema, 2020; Rosenfeld et al., 2020; Stephen Shankland, 2022). However, the development of such a treatment comes with significant challenges. The method of optimizing electrode placement that we present here addresses several of these challenges. It will optimize the design and placement of electrode arrays to obtain a functional implant with coverage and resolution that matches a preset target, within predetermined boundaries for surgical implantation.

Our data-driven solution simulates stimulation-evoked phosphenes based on individual anatomy and efficiently optimizes electrode placement to minimize the difference between the simulated phosphene patterns and a predetermined target layout. While the general method works for many different types of electrode arrays, we here present its characteristics for a 1000-channel 3D electrode array implant. Even though we asked the algorithm to optimize electrode placement in V1 specifically, some contact points still ended up in V2 and V3. The algorithm also has the capacity of optimizing placement based on multiple visual areas, but it is currently unknown how phosphenes that are evoked in distinct visual areas are perceptually combined into patterns. Future studies should address this question, as it would greatly expand the possible configurations for a visual prosthesis.

The optimally predicted phosphene maps were generally closer to the target distribution for the right hemisphere for all targets, except the inner target. This difference might be related to anatomical hemispheric differences (see also supplementary figure S1). Our results also demonstrated that while it is possible to base electrode placement on the optimization solution in the average brain, an individually optimized approach performed significantly better. This finding underscores the importance of tailoring electrode placement to the specific anatomical characteristics of each

individual. By considering individual variations, we can achieve better outcomes and optimize visual restoration for each patient.

Covering the entire visual field with high spatial resolution is an unrealistic goal with currently available electrodes such as the type of single rigid electrode grid we simulate here. It might be achieved by distributing electrodes over multiple (smaller) electrode arrays, but new optimization challenges emerge when trying to optimize the placement of multiple interdependent arrays, e.g., they cannot physically occupy the same space. Our current approach can easily be expanded to place multiple electrode arrays in a serial manner, but this may not yield the most optimal solution and more complex optimization procedures may be necessary. About half of the electrodes in our simulations were located inside grey matter with most of the remaining electrodes likely located in white matter. Here, we assumed that white matter stimulation cannot be used. This assumption is partly based on the lack of a clear prediction for the retinotopic organization of white matter. However, since these fiber paths do connect visual areas and carry visual information, further research might help to understand the perceptual manifestation of white matter stimulation.

The loss terms implemented in our approach were chosen for interpretability and ease of use, but they can easily be customized, replaced, or expanded, which makes the implant optimization framework rather flexible. With the example electrode array used here, optimization results were more successful for the foveal (inner) target region, compared to the more peripheral (full, upper and lower) target regions. This is a direct consequence of the higher eccentricities being located deeper along the calcarine and requiring longer shanks to reach them, which automatically increases the electrode spacing along the shank. In addition, a relatively large part of cortex is dedicated to central vision (low eccentricities) compared to peripheral vision (known as cortical magnification). A more suitable approach to get coverage from the peripheral visual field is to target different sections of the visual field with multiple electrode arrays and/or in different visual areas. Retinotopic maps are ubiquitous along the visual cortical hierarchy (Wandell et al., 2007), but receptive field sizes increase towards higher areas, reducing the spatial resolution of potential phosphene vision. Importantly, and to reiterate a previous point, it is currently unknown how simultaneous stimulation across hierarchically different visual areas perceptually combines.

The accuracy of the phosphene map predictions in our pipeline crucially depends on 1) the precision and the spatial resolution of the underlying population receptive field maps/atlas. There is an accumulative uncertainty that stems from alignment and extrapolating data from seeing individuals to blind individuals. 2) the assumptions of the phosphene simulation algorithm. A possible improvement could be to acquire higher quality pRF data. The availability of even higher field strengths could potentially yield scans with higher resolution. It is highly recommended to obtain detailed individual anatomy using a high-resolution MRI scan whenever possible. Retinotopy can then be estimated based on individual anatomy and group-average (probabilistic) pRF maps, yielding the best possible results. Finally, the current version of our optimization procedure does not account for intracranial vasculature, which is another practical constraint for implantation. Future versions of the pipeline might be expanded to also optimize the tissue that is crossed to reach the target location as a way to avoid larger vasculature. Such an approach would be a refinement, but it does require even more detailed structural scans of individual patients' brains.

In conclusion, we present an automated approach to optimize the selection of electrode placement for brain-based visual prostheses that finds the closest possible match to a preset visual field coverage. Our openly and freely available software (https://github.com/rickvanhoof/vimplant) can easily be expanded or adjusted to facilitate different electrode configurations (including multiple arrays), different target areas (including multiple areas), or different constraints (through different cost functions). As such, it will be able to refine surgical procedures as well as drive simulation studies in healthy observers with phosphene vision configurations that are realistic representations of the possibilities with any given electrode design.

REFERENCES

Avraham, D., Jung, J., Yitzhaky, Y., & Peli, E. (2021). Retinal prosthetic vision simulation: temporal aspects. *Journal of Neural Engineering*. https://doi.org/10.1088/1741-2552/AC1B6C

Beauchamp, M. S., Oswalt, D., Sun, P., Foster, B. L., Magnotti, J. F., Niketeghad, S., Pouratian, N., Bosking, W. H., & Yoshor, D. (2020). Dynamic Stimulation of Visual Cortex Produces Form Vision in Sighted and Blind Humans. *Cell*, *181*(4), 774-783.e5. https://doi.org/10.1016/J.CELL.2020.04.033

Benson, N. C., Butt, O. H., Brainard, D. H., & Aguirre, G. K. (2014). Correction of Distortion in Flattened Representations of the Cortical Surface Allows Prediction of V1-V3 Functional Organization from Anatomy. *PLOS Computational Biology*, *10*(3), e1003538. https://doi.org/10.1371/JOURNAL.PCBI.1003538

Benson, N. C., Jamison, K. W., Arcaro, M. J., Vu, A. T., Glasser, M. F., Coalson, T. S., Essen, D. C. Van, Yacoub, E., Ugurbil, K., Winawer, J., & Kay, K. (2018a). The Human Connectome Project 7 Tesla retinotopy dataset: Description and population receptive field analysis. *Journal of Vision*, *18*(13), 23–23. https://doi.org/10.1167/18.13.23

Benson, N. C., Jamison, K. W., Arcaro, M. J., Vu, A. T., Glasser, M. F., Coalson, T. S., Essen, D. C. Van, Yacoub, E., Ugurbil, K., Winawer, J., & Kay, K. (2018b). The Human Connectome Project 7 Tesla retinotopy dataset: Description and population receptive field analysis. *Journal of Vision*, *18*(13), 23–23. https://doi.org/10.1167/18.13.23

Benson, N. C., & Winawer, J. (2018). Bayesian analysis of retinotopic maps. *ELife*, *7*, 1–29.

Benson, N. C., Yoon, J. M. D., Forenzo, D., Engel, S. A., Kay, K. N., & Winawer, J. (2021). Variability of the Surface Area of the V1, V2, and V3 Maps in a Large Sample of Human Observers. *BioRxiv*, 2020.12.30.424856. https://doi.org/10.1101/2020.12.30.424856

Benson, N. C., Yoon, J. M. D., Forenzo, D., Engel, S. A., Kay, K. N., & Winawer, J. (2022). Variability of the Surface Area of the V1, V2, and V3 Maps in a Large Sample of Human Observers. *Journal of Neuroscience*, *42*(46), 8629–8646. https://doi.org/10.1523/JNEUROSCI.0690-21.2022

Bollen, C. J. M., Guclu, U., Van Wezel, R. J. A., Van Gerven, M. A. J., & Gucluturk, Y. (2019). Simulating neuroprosthetic vision for emotion recognition. *2019 8th International Conference on Affective Computing and Intelligent Interaction Workshops and Demos, ACIIW 2019*, 85–87. https://doi.org/10.1109/ACIIW.2019.8925229

Bosking, W. H., Oswalt, D. N., Foster, B. L., Sun, P., Beauchamp, M. S., & Yoshor, D. (2022). Percepts evoked by multi-electrode stimulation of human visual cortex. *Brain Stimulation*, *15*(5), 1163–1177. https://doi.org/10.1016/J.BRS.2022.08.007

Brindley, G. S., & Lewin, W. S. (1968). The sensations produced by electrical stimulation of the visual cortex. *The Journal of Physiology*, *196*(2), 479. https://doi.org/10.1113/JPHYSIOL.1968.SP008519

Chen, S., Suaning, G., Morley, J., & Lovell, N. (2009). Simulating prosthetic vision: I. Visual models of phosphenes. *Vision Research*, *49*(12), 1493–1506. https://doi.org/10.1016/J.VISRES.2009.02.003

Chen, X., Wang, F., Fernandez, E., & Roelfsema, P. R. (2020). Shape perception via a high-channel-count neuroprosthesis in monkey visual cortex. *Science*, *370*(6521), 1191–1196. https://doi.org/10.1126/SCIENCE.ABD7435

Chen, X., Wang, F., Kooijmans, R., Klink, P. C., Boehler, C., Asplund, M., & Roelfsema, P. R. (2023). Chronic stability of a neuroprosthesis comprising multiple adjacent Utah arrays in monkeys. *Journal of Neural Engineering*, *20*(3), 036039. https://doi.org/10.1088/1741-2552/ACE07E

de Ruyter van Steveninck, J., van Gestel, T., Koenders, P., van der Ham, G., Vereecken, F., van Gerven, M., Güçlütürk, Y., & van Wezel, R. (2022). Real-world indoor mobility with simulated prosthetic vision: The benefits and feasibility of contour-based scene simplification at different phosphene resolutions. *Journal of Vision*, *22*(2), 1–1. https://doi.org/10.1167/JOV.22.2.1

Dobelle, W. H., Mladejovsky, M. G., Evans, J. R., Roberts, T. S., & Girvin, J. P. (1976). Braille reading by a blind volunteer by visual cortex stimulation. *Nature*, *259*(5539), 111–112. https://doi.org/10.1038/259111a0

Dobelle, W. H., Mladejovsky, M. G., & Girvin, J. P. (1974). Artificial vision for the blind: Electrical stimulation of visual cortex offers hope for a functional prosthesis. *Science*, *183*(4123), 440–444. https://doi.org/10.1126/science.183.4123.440

Farnum, A., & Pelled, G. (2020). New Vision for Visual Prostheses. *Frontiers in Neuroscience*, *0*, 36. https://doi.org/10.3389/FNINS.2020.00036

Fernández, E., Alfaro, A., Soto-Sánchez, C., Gonzalez-Lopez, P., Lozano, A. M., Peña, S., Grima, M. D., Rodil, A., Gómez, B., Chen, X., Roelfsema, P. R., Rolston, J. D., Davis, T. S., & Normann, R. A. (2021). Visual percepts evoked with an intracortical 96-channel microelectrode array inserted in human occipital cortex. *The Journal of Clinical Investigation*, *131*(23). https://doi.org/10.1172/JCI151331

Gilissen, E., & Zilles, K. (1996). The calcarine sulcus as an estimate of the total volume of human striate cortex: a morphometric study of reliability and intersubject variability. *Journal Fur Hirnforschung*, *37*(1), 57–66. https://europepmc.org/article/med/8964978

Heitmann, C., Zhan, M., Linke, M., Hölig, C., Kekunnaya, R., van Hoof, R., Goebel, R., & Röder, B. (2023). Early visual experience refines the retinotopic organization within and across visual cortical regions. *Current Biology*, *33*(22), 4950-4959.e4. https://doi.org/10.1016/j.cub.2023.10.010

Horton, J. C., & Hoyt, W. F. (1991). The Representation of the Visual Field in Human Striate Cortex: A Revision of the Classic Holmes Map. *Archives of Ophthalmology*, *109*(6), 816–824. https://doi.org/10.1001/ARCHOPHT.1991.01080060080030

Li, H., Su, X., Wang, J., Kan, H., Han, T., Zeng, Y., & Chai, X. (2018). Image processing strategies based on saliency segmentation for object recognition under simulated prosthetic vision. *Artificial Intelligence in Medicine*, *84*, 64–78. https://doi.org/10.1016/J.ARTMED.2017.11.001

Lu, Y., Wang, J., Wu, H., Li, L., Cao, X., & Chai, X. (2014). Recognition of Objects in Simulated Irregular Phosphene Maps for an Epiretinal Prosthesis. *Artificial Organs*, *38*(2), E10–E20. https://doi.org/10.1111/AOR.12174

Macé, M. J.-M., Guivarch, V., Denis, G., & Jouffrais, C. (2015). Simulated Prosthetic Vision: The Benefits of Computer-Based Object Recognition and Localization. *Artificial Organs*, *39*(7), E102–E113. https://doi.org/10.1111/AOR.12476

Mundel, T., Milton, J. G., Dimitrov, A., Wilson, H. W., Pelizzari, C., Uftring, S., Torres, I., Erickson, R. K., Spire, J. P., & Towle, V. L. (2003). Transient inability to distinguish between faces: electrophysiologic studies. *Journal of Clinical Neurophysiology : Official Publication of the American Electroencephalographic Society*, *20*(2), 102–110. https://doi.org/10.1097/00004691-200304000-00003

Niketeghad, S., & Pouratian, N. (2019). Brain Machine Interfaces for Vision Restoration: The Current State of Cortical Visual Prosthetics. *Neurotherapeutics*, *16*(1), 134. https://doi.org/10.1007/S13311-018-0660-1

Nowik, K., Langwińska-Wośko, E., Skopiński, P., Nowik, K. E., & Szaflik, J. P. (2020). Bionic eye review – An update. *Journal of Clinical Neuroscience*, *78*, 8–19. https://doi.org/10.1016/J.JOCN.2020.05.041

Oswalt, D., Bosking, W., Sun, P., Sheth, S. A., Niketeghad, S., Salas, M. A., Patel, U., Greenberg, R., Dorn, J., Pouratian, N., Beauchamp, M., & Yoshor, D. (2021). Multi-electrode stimulation evokes consistent spatial patterns of phosphenes and improves phosphene mapping in blind subjects. *Brain Stimulation*, *14*(5), 1356–1372. https://doi.org/10.1016/J.BRS.2021.08.024

Pedregosa, F., Michel, V., Grisel, O., Blondel, M., Prettenhofer, P., Weiss, R., Vanderplas, J., Cournapeau, D., Pedregosa, F., Varoquaux, G., Gramfort, A., Thirion, B., Grisel, O., Dubourg, V., Passos, A., Brucher, M., Perrot, M., Duchesnay, É., & Duchesnay, F. (2011). Scikit-learn: Machine Learning in Python. *Journal of Machine Learning Research*, *12*, 2825–2830. http://scikit-learn.sourceforge.net.

Perez-Yus, A., Bermudez-Cameo, J., Guerrero, J. J., & Lopez-Nicolas, G. (2017). Depth and Motion Cues with Phosphene Patterns for Prosthetic Vision. *Proceedings - 2017 IEEE International Conference on Computer Vision Workshops, ICCVW 2017*, *2018-Janua*, 1516–1525. https://doi.org/10.1109/ICCVW.2017.179

Polimeni, J. R., Balasubramanian, M., & Schwartz, E. L. (2006). Multi-area visuotopic map complexes in macaque striate and extra-striate cortex. *Vision Research*, *46*(20), 3336–3359. https://doi.org/10.1016/J.VISRES.2006.03.006

Roelfsema, P. R. (2020). Writing to the Mind's Eye of the Blind. *Cell*, *181*(4), 758–759. https://doi.org/10.1016/J.CELL.2020.03.014

Rosenfeld, J., Wong, Y., Yan, E., & Lowery, A. (2020). Tissue response to a chronically implantable wireless intracortical visual prosthesis (Gennaris array). *Iopscience.Iop.Org*. https://iopscience.iop.org/article/10.1088/1741-2552/ab9e1c/meta

Rosenke, M., van Hoof, R., van den Hurk, J., Grill-Spector, K., & Goebel, R. (2021). A Probabilistic Functional Atlas of Human Occipito-Temporal Visual Cortex. *Cerebral Cortex*, *31*(1), 603–619. https://doi.org/10.1093/CERCOR/BHAA246

Salzman, C. D., Britten, K. H., & Newsome, W. T. (1990). Cortical microstimulation influences perceptual judgements of motion direction. *Nature 1990 346:6280*, *346*(6280), 174–177. https://doi.org/10.1038/346174a0

Sanchez-Garcia, M., Martinez-Cantin, R., & Guerrero, J. J. (2018). *Structural and object detection for phosphene images*. http://arxiv.org/abs/1809.09607

Sanchez-Garcia, M., Martinez-Cantin, R., & Guerrero, J. J. (2020). Semantic and structural image segmentation for prosthetic vision. *PLOS ONE*, *15*(1), e0227677. https://doi.org/10.1371/JOURNAL.PONE.0227677

Schiller, P. H., Slocum, W. M., Kwak, M. C., Kendall, G. L., & Tehovnik, E. J. (2011). New methods devised specify the size and color of the spots monkeys see when striate cortex (area V1) is electrically stimulated. *Proceedings of the National Academy of Sciences of the United States of America*, *108*(43), 17809–17814. https://doi.org/10.1073/PNAS.1108337108/SUPPL_FILE/PNAS.201108337SI.PDF

Schmidt, E. M., Bak, M. J., Hambrecht, F. T., Kufta, C. V., O'Rourke, D. K., & Vallabhanath, P. (1996). Feasibility of a visual prosthesis for the blind based on intracortical micro stimulation of the visual cortex. *Brain*, *119*(2), 507–522. https://doi.org/10.1093/BRAIN/119.2.507

Schwartz, E. L. (1983). Cortical mapping and perceptual invariance: A reply to cavanagh. *Vision Research*, *23*(8), 831–835. https://doi.org/10.1016/0042-6989(83)90206-7

Seabold, S., & Perktold, J. (2010). *statsmodels: Econometric and statistical modeling with python*. In 9th Python in Science Conference.

Shahriari, B., Swersky, K., Wang, Z., Adams, R. P., & De Freitas, N. (2016). Taking the human out of the loop: A review of Bayesian optimization. *Proceedings of the IEEE*, *104*(1), 148–175. https://doi.org/10.1109/JPROC.2015.2494218

Stephen Shankland. (2022). *Neuralink's Upgraded Brain Chip Hopes to Help the Blind See and the Paralyzed Walk - CNET*. https://www.cnet.com/science/neuralink-upgraded-brain-chip-hopes-to-help-the-blind-see-and-the-paralyzed-walk/

Steveninck, J. de R. van, Güçlü, U., Wezel, R. van, & Gerven, M. van. (2020). End-to-end optimization of prosthetic vision. *BioRxiv*, 2020.12.19.423601. https://doi.org/10.1101/2020.12.19.423601

Tehovnik, E. J., Slocum, W. M., Carvey, C. E., & Schiller, P. H. (2005). Phosphene Induction and the Generation of Saccadic Eye Movements by Striate Cortex. *Https://Doi.Org/10.1152/Jn.00736.2004*, *93*(1), 1–19. https://doi.org/10.1152/JN.00736.2004

Tehovnik, E. J., Tolias, A. S., Sultan, F., Slocum, W. M., & Logothetis, N. K. (2006). Direct and indirect activation of cortical neurons by electrical microstimulation. *Journal of Neurophysiology*, *96*(2), 512–521. https://doi.org/10.1152/JN.00126.2006/ASSET/IMAGES/LARGE/Z9K0080675760003.JPEG

Maureen van der Grinten, Jaap de Ruyter van Steveninck, Antonio Lozano, Laura Pijnacker, Bodo Rueckauer, Pieter Roelfsema, Marcel van Gerven, Richard van Wezel, Umut Güçlü, Yağmur Güçlütürk (2024) Towards biologically plausible phosphene simulation for the differentiable optimization of visual cortical prostheses eLife 13:e85812. https://doi.org/10.7554/eLife.85812

Vergnieux, V., Macé, M. J.-M., & Jouffrais, C. (2017). Simplification of Visual Rendering in Simulated Prosthetic Vision Facilitates Navigation. *Artificial Organs*, *41*(9), 852–861. https://doi.org/10.1111/AOR.12868

Virtanen, P., Gommers, R., & Oliphant, T. E. (2020). SciPy 1.0: fundamental algorithms for scientific computing in Python. *Nature Methods*, *17*(3), 261–272. https://doi.org/10.1038/S41592-019-0686-2

Wandell, B., Dumoulin, S., & Brewer, A. (2007). Visual Field Maps in Human Cortex. *Neuron*, *56*(2), 366–383. https://doi.org/10.1016/J.NEURON.2007.10.012

Wang, J., Zhu, H., Liu, J., Li, H., Han, Y., Zhou, R., & Zhang, Y. (2021). The application of computer vision to visual prosthesis. *Artificial Organs*. https://doi.org/10.1111/AOR.14022

Wang, L., Mruczek, R. E. B., Arcaro, M. J., & Kastner, S. (2015). Probabilistic Maps of Visual Topography in Human Cortex. *Cerebral Cortex*, *25*(10), 3911–3931. https://doi.org/10.1093/CERCOR/BHU277

Wang, L., Yang, L., & Dagnelie, G. (2008). Virtual Wayfinding Using Simulated Prosthetic Vision in Gaze-locked Viewing. *Optometry and Vision Science : Official Publication of the American Academy of Optometry*, *85*(11), E1057. https://doi.org/10.1097/OPX.0B013E31818B9F36

Xia, P., Hu, J., & Peng, Y. (2015). Adaptation to Phosphene Parameters Based on Multi-Object Recognition Using Simulated Prosthetic Vision. *Artificial Organs*, *39*(12), 1038–1045. https://doi.org/10.1111/AOR.12504

Yang, G., Zhou, S., Bozek, J., Dong, H. M., Han, M., Zuo, X. N., Liu, H., & Gao, J. H. (2020). Sample sizes and population differences in brain template construction. *NeuroImage*, *206*, 116318. https://doi.org/10.1016/J.NEUROIMAGE.2019.116318

de Ruyter van Steveninck, J., van Gestel, T., Koenders, P., van der Ham, G., Vereecken, F., van Gerven, M., Güçlütürk, Y., & van Wezel, R. (2022). Real-world indoor mobility with simulated prosthetic vision: The benefits and feasibility of contour-based scene simplification at different phosphene resolutions. *Journal of Vision*, *22*(2), 1–1. https://doi.org/10.1167/JOV.22.2.1

Fernández, E., Alfaro, A., Soto-Sánchez, C., Gonzalez-Lopez, P., Lozano, A. M., Peña, S., Grima, M. D., Rodil, A., Gómez, B., Chen, X., Roelfsema, P. R., Rolston, J. D., Davis, T. S., & Normann, R. A. (2021). Visual percepts evoked with an intracortical 96-channel microelectrode array inserted in human occipital cortex. *The Journal of Clinical Investigation*, *131*(23). https://doi.org/10.1172/JCI151331

Horton, J. C., & Hoyt, W. F. (1991). The Representation of the Visual Field in Human Striate Cortex: A Revision of the Classic Holmes Map. *Archives of Ophthalmology*, *109*(6), 816–824. https://doi.org/10.1001/ARCHOPHT.1991.01080060080030

Lu, Y., Wang, J., Wu, H., Li, L., Cao, X., & Chai, X. (2014). Recognition of Objects in Simulated Irregular Phosphene Maps for an Epiretinal Prosthesis. *Artificial Organs*, *38*(2), E10–E20. https://doi.org/10.1111/AOR.12174

Perez-Yus, A., Bermudez-Cameo, J., Guerrero, J. J., & Lopez-Nicolas, G. (2017). Depth and Motion Cues with Phosphene Patterns for Prosthetic Vision. *Proceedings - 2017 IEEE International Conference on Computer Vision Workshops, ICCVW 2017*, *2018-Janua*, 1516–1525. https://doi.org/10.1109/ICCVW.2017.179

Polimeni, J. R., Balasubramanian, M., & Schwartz, E. L. (2006). Multi-area visuotopic map complexes in macaque striate and extra-striate cortex. *Vision Research*, *46*(20), 3336–3359. https://doi.org/10.1016/J.VISRES.2006.03.006

Roelfsema, P. R. (2020). Writing to the Mind's Eye of the Blind. *Cell*, *181*(4), 758–759. https://doi.org/10.1016/J.CELL.2020.03.014

Rosenfeld, J., Wong, Y., Yan, E., & Lowery, A. (2020). Tissue response to a chronically implantable wireless intracortical visual prosthesis (Gennaris array). *Iopscience.Iop.Org*. https://iopscience.iop.org/article/10.1088/1741-2552/ab9e1c/meta

Schwartz, E. L. (1983). Cortical mapping and perceptual invariance: A reply to cavanagh. *Vision Research*, *23*(8), 831–835. https://doi.org/10.1016/0042-6989(83)90206-7

Seabold, S., & Perktold, J. (2010). *statsmodels: Econometric and statistical modeling with python*. In 9th Python in Science Conference.

Stephen Shankland. (2022). *Neuralink's Upgraded Brain Chip Hopes to Help the Blind See and the Paralyzed Walk - CNET*. https://www.cnet.com/science/neuralink-upgraded-brain-chip-hopes-to-help-the-blind-see-and-the-paralyzed-walk/

Tehovnik, E. J., Tolias, A. S., Sultan, F., Slocum, W. M., & Logothetis, N. K. (2006). Direct and indirect activation of cortical neurons by electrical microstimulation. *Journal of Neurophysiology*, *96*(2), 512–521. https://doi.org/10.1152/JN.00126.2006/ASSET/IMAGES/LARGE/Z9K0080675760003.JPEG

Van Der Grinten, M., De Ruyter Van Steveninck, J., Lozano, A., Pijnacker, L., Rückauer, B., Roelfsema, P., Van Gerven, M., Van Wezel, R., Güçlü, U., & Gmur Güçlütürk, Y. ˘. (2022). Biologically plausible phosphene simulation for the differentiable optimization of visual cortical prostheses. *BioRxiv*, 2022.12.23.521749. https://doi.org/10.1101/2022.12.23.521749

Biologically plausible phosphene simulation for the differentiable optimization of visual cortical prostheses. *Biorxiv.Org*. https://doi.org/10.1101/2022.12.23.521749

Vergnieux, V., Macé, M. J.-M., & Jouffrais, C. (2017). Simplification of Visual Rendering in Simulated Prosthetic Vision Facilitates Navigation. *Artificial Organs*, *41*(9), 852–861. https://doi.org/10.1111/AOR.12868

Wang, L., Yang, L., & Dagnelie, G. (2008). Virtual Wayfinding Using Simulated Prosthetic Vision in Gaze-locked Viewing. *Optometry and Vision Science : Official Publication of the American Academy of Optometry*, *85*(11), E1057. https://doi.org/10.1097/OPX.0B013E31818B9F36